Rethinking sinking: Imaging the flow fields of natural marine aggregates to derive sinking velocity

Clara M. Flintrop[1,2,#,*], Soeren Ahmerkamp[3,#,*], Nasrollah Moradi[3,4], Isabell Klawonn[5,6], Jöran März[7], Cora Hörstmann[2,3,8], Rainer Kiko[9], Arzhang Khalili[3], Hans-Peter Grossart[5,10], Xosé A. Álvarez-Salgado[11], Javier Aristegui[12], Morten H. Iversen[2,4]

[#]Authors have contributed equally

*Corresponding author e-mail: clara.flintrop@mail.huji.ac.il, sahmerka@mpi-bremen.de

[1]The Fredy & Nadine Herrmann Institute of Earth Sciences, Hebrew University of Jerusalem, Jerusalem 91904, Israel; Interuniversity Institute for Marine Sciences, Eilat 88103, Israel

[2]Alfred Wegener Institute, Helmholtz Centre for Polar and Marine Research, 27570 Bremerhaven, Germany.

[3]Department of Biogeochemistry, Max-Planck-Institute for Marine Microbiology, 28359 Bremen, Germany

[4]MARUM and University of Bremen, 28359 Bremen, Germany

[5]Department of Plankton and Microbial Ecology, Leibniz-Institute for Freshwater Ecology and Inland Fisheries (IGB), 12587 Berlin, Germany

[6]Department of Biological Oceanography, Leibniz Institute for Baltic Sea Research Warnemünde (IOW), 18119 Rostock, Germany

[7]University of Bergen, Geophysical Institute and Bjerknes Centre for Climate Research, 5007 Bergen, Norway

[8]Mediterranean Institute of Oceanography (MIO), 13009 Marseille, France

[9]GEOMAR Helmholtz Centre for Ocean Research, 24148 Kiel, Germany

[10]Potsdam University, Institute of Biochemistry and Biology, 14469 Potsdam Germany

[11]Instituto de Investigacións Mariñas-CSIC, 36208 Vigo, Spain

[12]Instituto de Oceanografía y Cambio Global (IOCAG), Universidad de Las Palmas de Gran Canaria, 35214 Telde, Las Palmas de Gran Canaria, Spain

Key words: marine snow, aggregate porosity, Particle Image Velocimetry (PIV), Stokes' law, carbon flux

Running head: Contribution of small particles to carbon flux

Abstract

The marine biological carbon pump is driven by the interplay between particle sinking velocity and remineralisation. Despite its importance, sinking velocity of natural marine aggregates is not routinely measured, but often calculated from aggregate size and density using Stokes' law. Yet, comparing calculated and experimentally measured sinking velocities has shown that Stokes' law does not accurately predict the size-to-sinking relationship of marine aggregates because size-dependent changes in porosity are not well considered. We analysed the flow fields around 81 *in situ* collected aggregates using Particle Image Velocimetry (PIV) in order to determine the controlling factors for aggregate settling and provide a better scaling for their porosity. The flow

fields around all types and sizes of aggregates strongly resembled those of impermeable, porous spheres. Using an independently derived scaling of porosity with size, we could accurately predict the sinking velocity of laboratory- and field-collected aggregates with known density. Our improved sinking velocity calculations provide carbon flux predictions that matched measured flux well, while flux calculated with sinking velocity calculations using Stokes' law underestimated flux on average by 2-fold. When applying our improved estimates for settling velocity to a global data set of vertical particle abundance and size-distribution, our findings reveal that small particles (< 500 µm) contribute 40% to total carbon flux in high latitudes and 70% in equatorial regions. This substantial contribution of small particles to total carbon fluxes across various oceans has previously been attributed to their high numerical abundances. Here, we provide a mechanistic basis for this phenomenon, i.e., their relatively low porosities render them compact and dense particles with high size-specific settling velocities and thus a high carbon-to-volume ratio.

Introduction

Sinking of phytoplankton cells to the deep ocean in the form of marine snow (aggregated phytoplankton and detritus > 500 µm) or as zooplankton faecal pellets causes an average carbon flux of 5-12 PgC yr^{-1} out of the sea surface (Fender et al. 2022 and references therein). The efficiency of this process, known as the biological carbon pump (BCP; Volk and Hoffert 1985), is regulated by heterotrophic organisms in the water column (Grossart and Ploug 2001; Simon et al. 2002). The amount of biotic remineralisation, and thus carbon flux attenuation, is strongly related to aggregate sinking velocity because it determines the residence time of aggregates in the upper

1000 m and thereby the time available for degradation (Iversen and Ploug 2010; Morten Hvitfeldt Iversen et al. 2010; Cavan et al. 2017; Bach et al. 2016). Natural marine snow has high remineralisation rates, and typically 80% of the POC contained within a slow-sinking aggregate is remineralised in the first 200 m of the water column (Ploug et al. 1999; Grossart and Ploug 2001). Despite the significance of sinking velocity for export flux, this parameter is not routinely measured. Direct measurements of aggregate sinking velocity are time-consuming and require collection of intact *in situ* formed aggregates (Riley et al. 2012). Several methods are used to measure aggregate sinking velocity, e.g., net-jet flow systems (Ploug and Jørgensen 1999; Ploug et al. 2008; Iversen and Ploug 2010), sinking columns (Silver et al. 1984; Gorsky et al. 1984; Hansen et al. 1996), and roller tanks (Engel and Schartau 1999; Ploug et al. 2010). However, direct measurements of sinking velocity for *in situ* formed aggregates are rare because of restrictions imposed by sampling depth and processing time. *In situ* camera systems like the Underwater Velocity Profiler (UVP; Stemmann et al. 2004; Picheral et al. 2010) have become the gold standard for high-throughput vertical profiling of particle abundance -, volume -, and size spectra (see Giering et al. [2020] for a comprehensive overview of optical systems). Although optical systems do not routinely measure sinking velocity, they are often used for carbon flux calculations by assuming that aggregate size scales as a power function to both sinking velocity and mass (Guidi et al. 2015, 2008; Iversen et al. 2010).

To indirectly determine flux using *in situ* camera profiles, aggregate sinking velocity is calculated according to Stokes' law (Jackson and Checkley 2011, Stokes 1851), where sinking velocity is a function of the squared particle radius and the excess density. However, it has been observed

that sinking velocities calculated using Stokes' law tend to underestimate the sinking velocity of smaller aggregates while overestimating the velocity of larger aggregates (e.g., Stemmann et al. 2004). Several properties of marine snow, including its highly variable morphology, surface roughness, and porosity, have been considered to explain the non-compliance with Stokes' law (Williams 1966; Matsumoto and Suganuma 1977; Baba and Komar 1981; Alldredge and Gotschalk 1988; Li and Logan 2001; Laurenceau-Cornec et al. 2015; Laurenceau-Cornec et al. 2020). Deviation from Stokes' law due to aggregate heterogeneity makes it difficult to determine a global relationship between size and sinking (e.g., McDonnell and Buesseler 2010; Iversen et al. 2010). Still, if aggregate density and porosity is considered, we hypothesize that general relationships can be identified when testing Stokes' sinking for different types of aggregates. We used Particle Image Velocimetry (PIV) to visualise the flow field around *in situ* collected aggregates and impermeable agar spheres, which we used as reference for Stokes-compliant particles. We compared measured sinking velocities to Stokes' prediction, and related sinking behaviour to the aggregates' and agar spheres' hydrodynamic flow field and physical parameters including size, porosity, density, structure, and composition to determine the factors controlling aggregate sinking velocity and improve existing parameterisations.

Results

Particle type, size and sinking velocity

The study was carried out in July and August 2017 in the North-West African Eastern Boundary Upwelling System during the campaign "Fluxes I" on board B/O Sarmiento de Gamboa (Fig. 1a). During the expedition we collected a total of 109 aggregates, which ranged in size from 0.38 to

3.56 mm (mean size 1.15 mm±0.65 SD) in equivalent spherical diameter. Based on their main constituents, we could assign 93 aggregates to three separate categories: phytoplankton aggregates, degraded faecal pellets, and ballasted mucous aggregates (Fig. 1b). Phytoplankton aggregates made up 45% of the total particle numbers and were distinguished from other aggregates by their heterogeneous composition, which included diatom chains, Acantharia, Radiolaria, mucilaginous particles from discarded feeding webs, fresh and degraded faecal pellets, copepod carcasses, and other unidentified phyto- and zoo-detritus. Twenty-seven percent of the aggregates were categorised as faecal pellets at various stages of degradation based on particle size, homogeneous distribution of matter, uniform coloring, and the oval shape (from here on also referred to as "faecal pellets"). A further 27% were categorised as ballasted mucous aggregates as they were comprised of a translucent, mucilaginous substance, possibly originating from discarded zooplankton feeding webs (from here on also referred to as "mucous aggregates"). Average grey value distributions of particles showed distinct differences between categories, allowing a semi-quantitative classification of particles from these distributions alone (Fig. S3a). Sinking velocities ranged from 50 to 410 meters per day (mean sinking velocity 156 m d^{-1}±74 SD). Albeit on the high side, this is comparable to previous measurements in the region (Fig. S1a). Agar sphere sinking velocity increased linearly with size, but there was no apparent correlation between size and sinking velocity for *in situ* collected aggregates, even after categorising particles based on their composition (Fig. S1b).

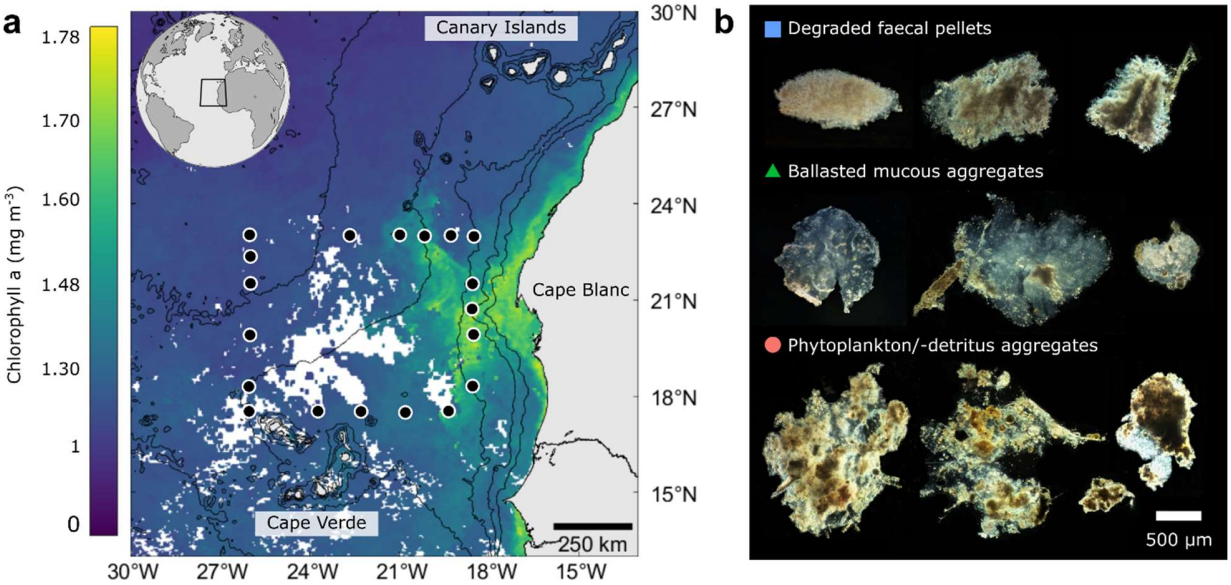

Figure 1. a) Sampling stations (black dots) and sea surface chlorophyll a concentration during the sampling period. **b)** Examples of the different types of particles collected in situ.

Flow fields around sinking marine snow

We analysed the flow fields around 81 *in situ*-collected particles of varying composition and structure using Particle Image Velocimetry (PIV). As reference for Stokes-compliant particles, we also analysed the flow fields of 13 agar spheres representing perfectly spherical, impermeable spheres. To compare the flow fields for different sinking velocities and aggregate sizes, we calculated their Reynolds numbers (*Re*), which ranged from 0.4 to 5.2 (mean *Re* 1.9±1.2 SD). This Reynolds number regime represents an intermediate range above creeping flow conditions ($Re \ll 1$) and far below a turbulent regime ($Re > 2300$). For $Re \sim 1$, the flow field was mostly symmetric, i.e., the velocity boundary layer thickness in front of the aggregate equaled the lee side boundary layer thickness, with only small variations. With increasing *Re*, the flow field became increasingly asymmetric. At similar *Re*, the flow fields of agar spheres and marine aggregates of various shapes and composition matched well (Fig. 2).

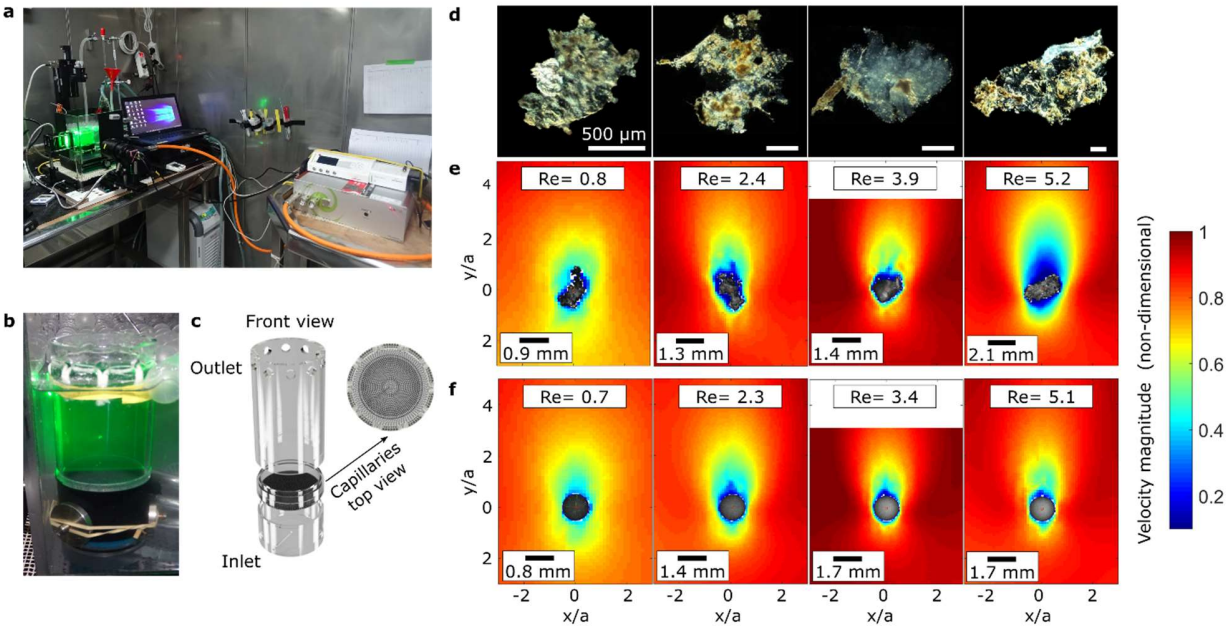

Figure 2. Left-hand column: **a)** Flow chamber set-up on board B/O Sarmiento de Gamboa. **b)** Aggregate is freely suspended in the flow chamber and illuminated by a pulsed light sheet (green) for PIV. **c** Modified design of the flow chamber for optimised laminar flow. Right-hand column: velocity magnitude inferred from the PIV results for various Reynolds numbers – **d** *In situ* collected particles with their corresponding flow fields (**e**). **f** Flow field comparison with agar spheres with comparable Reynolds number.

Scaling of boundary layer thickness and drag coefficient with Reynolds number

To quantify variations in the flow field for different *Re* regimes, we measured the thickness of the velocity boundary layer at the aggregate equator, defined as the fluid layer at the aggregate surface where flow velocity was ≤ 90% of the bulk flow velocity. Scaled boundary layer thickness, i.e., boundary layer thickness normalized by the x-axis diameter $(\delta_s = \delta/d)$ ranged from 0.37 to 2.11, and increased the apparent aggregate diameter up to 5-fold (Fig. 3a). There were no obvious patterns of deviation from the regression lines fitted for agar spheres and the *in situ* collected

aggregates, except that with increasing *Re* (starting around $Re = 3$), the boundary layer of aggregates became relatively thinner compared to that of agar spheres. Irrespective of aggregate type, boundary layer thickness scaled with *Re* following a power law ($\delta_s = 1.37 \cdot Re^{-0.46}$). *In situ* collected aggregates had irregular shapes and rough surfaces (Fig. 1b, Fig. S2b), but there was no significant difference between the power law coefficients for agar spheres ($\delta_s = 1.45 \cdot Re^{-0.48}$) and any of the aggregate types. To analyse the extent to which the deviation between theory and our measurements affected sinking velocity prediction, the drag coefficient C_D was estimated based on the measured boundary layer thickness (Material and Methods, Eq. 13). Generally, the drag coefficients for marine aggregates and agar spheres scaled with *Re* as expected from Stokes' law (Fig. 3b) with a best fit of

$$C_D = \frac{24}{Re^{0.8}} \qquad 1$$

Residuals between estimated drag coefficients and predicted drag coefficients were calculated as $((C_D - C_{D\ Agar\ spheres})/C_{D\ Agar\ spheres})$. Residuals were largest for small Reynolds numbers (*Re* < 1.5), i.e. large boundary layer thickness, where the drag coefficient is underestimated by Stokes' law (up to 5-fold, on average 2-fold). This deviation translates into an overestimation of the sinking velocity by 40% - 120% when calculated using Stokes' law. For larger Reynolds numbers (*Re* > 1.5), the residuals strongly decreased in magnitude (up to 2-fold, in average 1.5-fold), translating into sinking velocity overestimation of 20% - 40% when calculated with Stokes' law. By following the White extension for the drag coefficient (White 1974), the residuals further decreased by an average of 30% across the whole range of Reynolds numbers and the trend towards overestimation of sinking velocity for large aggregates was diminished. The magnitude of the residuals could not be explained by any of the measured individual aggregate properties.

Residuals varied between the different aggregate types, showing that Stokes Law was better at predicting the sinking velocity of some aggregate types, especially in the low Reynolds number (*Re* < 1.5) range. Residuals increased for certain shape parameters, but the effect was not statistically significant due to the large scatter amongst the aggregates of similar types (Fig. S2). The average error in predicting sinking velocity based on the White drag coefficient was estimated to be 10% for degraded faecal pellets, 16% for phytoplankton aggregates, and 26% for ballasted mucous aggregates.

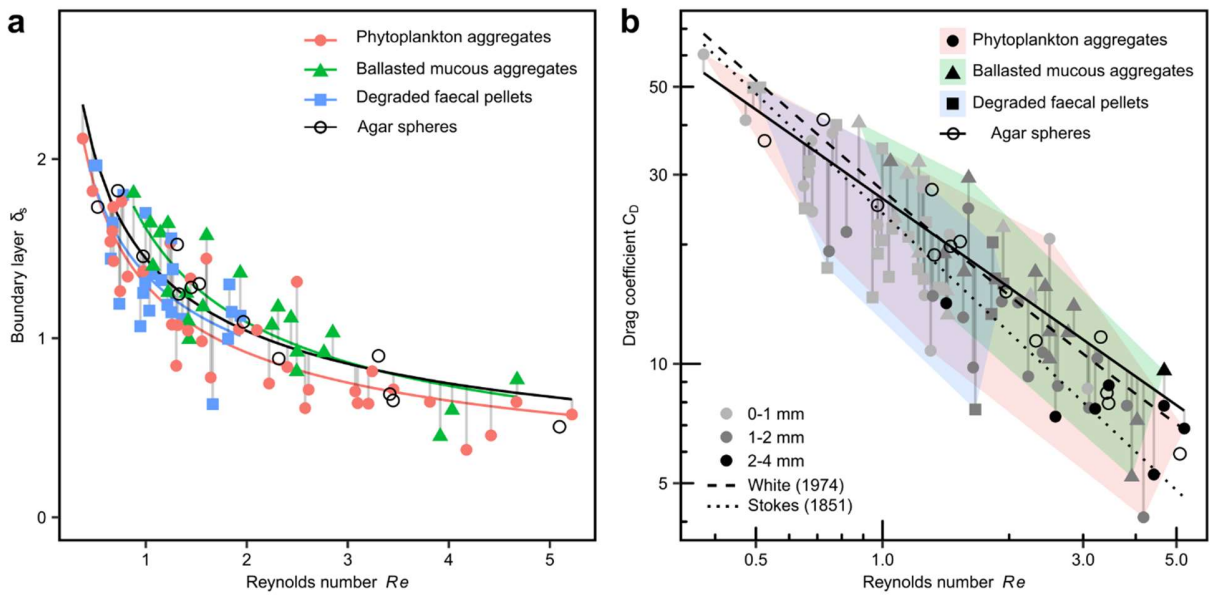

Figure 3. Relationship between Reynolds number and **a)** scaled equatorial boundary layer δ_s, and **b)** δ_s–based drag coefficient (Material and Methods, Eq. 13), for the different aggregate types and agar spheres.

Excess density, porosity, and fractality

The excess density of aggregates depends on the density of the solid fraction (solid hydrated density, ρ_{shd}) and the water density ρ_w, related to the porosity ϕ (Material and Methods, Eq. 14).

While solid hydrated density could be measured directly, we estimated the excess density using Eq. 12 (Material and Methods), where the boundary layer-estimated drag coefficient (C_D) was used to avoid circular reasoning. We found the excess density to range over two orders of magnitude from 0.0002 g cm^{-3} to 0.0209 g cm^{-3} (Table 1). Measured solid hydrated densities ranged from 1.119 g cm^{-3} to 1.430 g cm^{-3}, only explaining a minor fraction of the variability in excess densities (Table 1). Porosity ranged from 0.859 to 0.999, pointing to a large water fraction in the interstitials of the aggregates (Table 1). The volume fraction made up by solid material ranged from 0.141 to 0.001 encompassing two orders of magnitude and thereby explaining most of the observed variability of the excess densities. Averaged over all aggregate types, the amount of the solid fraction was related to the diameter of the aggregate by a power law function (Fig. 4a):

$$1 - \varphi = 0.02 \cdot d^{-1.71} \qquad 2$$

This implies that larger aggregates had an increased porosity, and therefore a reduced excess density (Fig. 4b). This behaviour is expected when taking fractal theories as a basis. The 1-dimensional fractal number (DF1) (inferred from the log-log relationship between perimeter and diameter according to Kilps et al. [1994]) indicates the roughness of the outer structure relative to a smooth sphere. Values around unity indicate a smooth surface, while larger numbers indicate uneven surfaces with structures that may reach into the boundary layer surrounding the aggregates. Agar spheres showed smooth outer structures with a DF1 of 0.73. Degraded faecal pellets and ballasted mucous aggregates had an intermediate roughness with DF1 values of 0.92 and 0.93. Phytoplankton aggregates had the largest DF1 with a value of 1.35. The 2-dimensional fractal number (DF2) (inferred from the log-log relationship between diameter and area according to Kilps et al. [1994]) relates the area of the aggregate to the area of a sphere with the same

diameter. Values of DF2 varied between 1.2 and 2, and, like aggregate diameter, DF2 values correlated with the fraction of solids in the aggregates (Table S1). Despite variations in fractal dimensions between different aggregate types, we observed a strong correlation between excess density and porosity:

$$\Delta\rho = 0.08 \cdot (1 - \varphi)^{0.73} \qquad 3$$

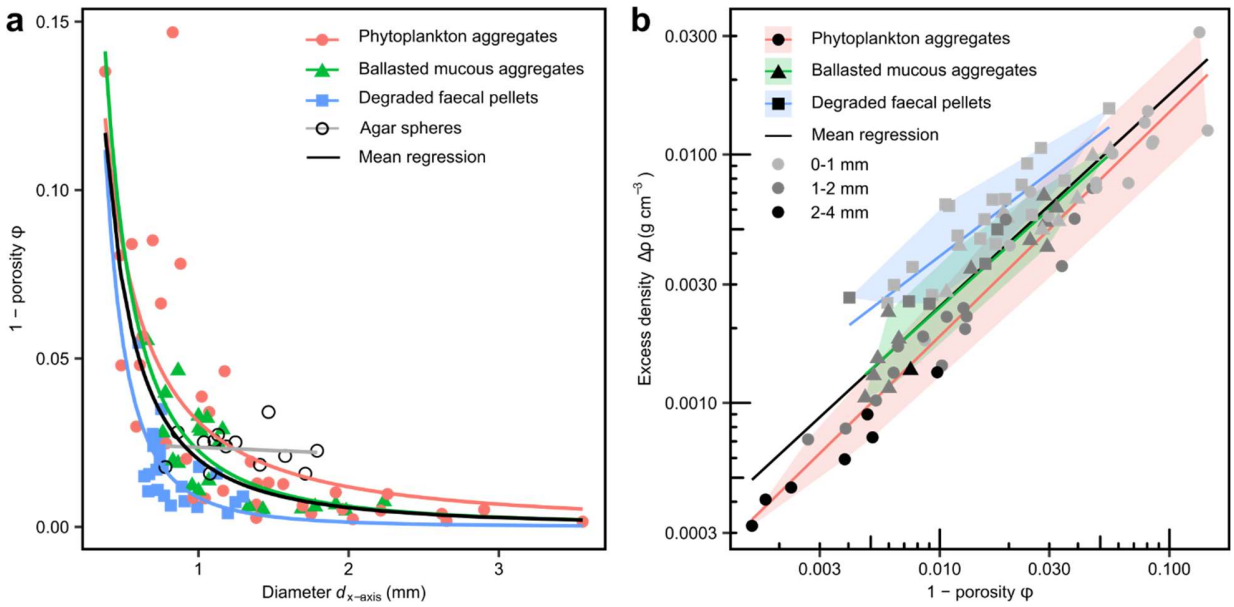

Figure 4. a) Relationship between aggregate solid fraction and aggregate size for different aggregate types and agar spheres. **b)** Relationship between aggregate solid fraction, aggregate excess density, and aggregate size for different aggregate types.

In situ particle carbon content and fluxes

To obtain the *in situ* carbon content of marine snow, we deployed drifting sediment traps at water depths of 100 m and 200 m for a duration of 22 hours (see Table S4). The drifting trap was equipped with gel traps and sediment traps, enabling us to determine the carbon fluxes and size-

spectrum of the *in situ* collected marine snow. The *in situ* measured total organic carbon and fluxes were relatively consistent with 42 mg C m^{-2} d^{-1}. To determine the size-specific carbon content of marine snow, we utilized the gel-trap particle numbers from specific size bins (see Material and Methods) and calculated the biovolume B (mm^3) as a function of equivalent circular diameter d, $B(d) = \frac{1}{6}\pi d^3$, assuming a spherical shape of the particles. Subsequently, we applied our size-dependent porosity (φ) relationship (Eq. 2) to estimate the solid fraction of the biovolume. By assuming that all the measured carbon is equally distributed, we determined the relationship between carbon content and biomass as

$$m(d) = 0.1524 \cdot \varphi\, B(d)^{-0.61} \qquad 4$$

Where m(d) is carbon content (µg mm^{-3}). When expressed as particle-specific carbon-content (µg $particle^{-1}$) per size bin, this relationship changes to $m(d) \propto B(d)^{0.39}$ which is slightly lower than a previously determined scaling of $m(d) \propto B(d)^{0.52}$ based on direct carbon measurements of single particles from the Peruvian upwelling region (Karthäuser et al. 2021).

Regional and global sinking velocity and carbon flux predictions

The newly derived size-dependent relationships for sinking velocity (Material and Methods, Eq. 16) and carbon content (Eq. 4) provide a means to determine i) porosity and—if solid hydrated density is measured or known from literature (Table S5) —sinking velocity based on aggregate size, and ii) carbon fluxes based on *in situ* measured size spectra. To test the validity of our model, we compared measured and predicted sinking velocities of aggregates with known solid hydrated density formed in the laboratory and collected *in situ*, including aggregates collected on this cruise. We found an overall good correlation between measured and predicted sinking velocities

of aggregates collected on this cruise ($w_{predicted}$=1.13·$w_{measured}$, adj. R2=-1.1), although there was a trend towards overestimating sinking velocities when predicted using Eq. 16 (Material and Methods), which was up to 2.5-fold for some aggregates (Fig. 5a). We also found a positive correlation between measured and predicted sinking velocities of *in situ*-collected and laboratory-formed aggregates from different studies ($w_{predicted}$=1.38·$w_{measured}$, adj. R2=0.03) (Fig. 5b). Here, too, large variabilities were observed, with the predicted sinking velocity being overestimated for some aggregates (up to 3-fold), and underestimated for others (up to 5-fold) (Fig. 5b).

To test the validity of our carbon content and carbon flux predictions, we averaged 72 particle profiles recorded with the UVP during the same cruise and utilized our relationships (Eq. 2, Eq. 4 and Eq. 14 [Material and Methods]) to calculate carbon fluxes and to assess the contribution of specific size classes to the overall carbon flux. The overall carbon flux at 100 m and 200 m was estimated to be 24 mg m^{-2} d^{-1} and 35 mg m^{-2} d^{-1}, respectively, which is on average 2-fold higher than predicted based on Stokes' law, but consistent with the sediment trap data. Intriguingly, our estimations indicate that small particles (<500 µm) contribute a remarkable 80% of the overall carbon flux (Fig. 5d). This proportion is substantially higher than the 9% predicted by Stokes' law, highlighting the significant role of abundant small particles for ocean carbon fluxes. In order to assess the persistent impact of small particles on carbon fluxes in larger regions, we conducted a thorough analysis utilizing 2,669 underwater-vision (UVP)-based particle profiles obtained from the publicly available ECOTAXA database (see Material and Methods). Carbon fluxes were determined at 1000 m depth, ranging from 2.3 mg m^{-2} d^{-1} (10th percentile) to 12.7 mg m^{-2} d^{-1} (90th percentile) on a global scale. Our findings revealed that small particles contribute 67% to

the global average carbon fluxes at the base of the annual mean mixed layer (Fig. 6). Notably, distinct meridional differences were observed, with the highest contribution of small particle fluxes occurring at 20° N/S (81-85%) and a still significant contribution of 46% to 50% at 65° N/S.

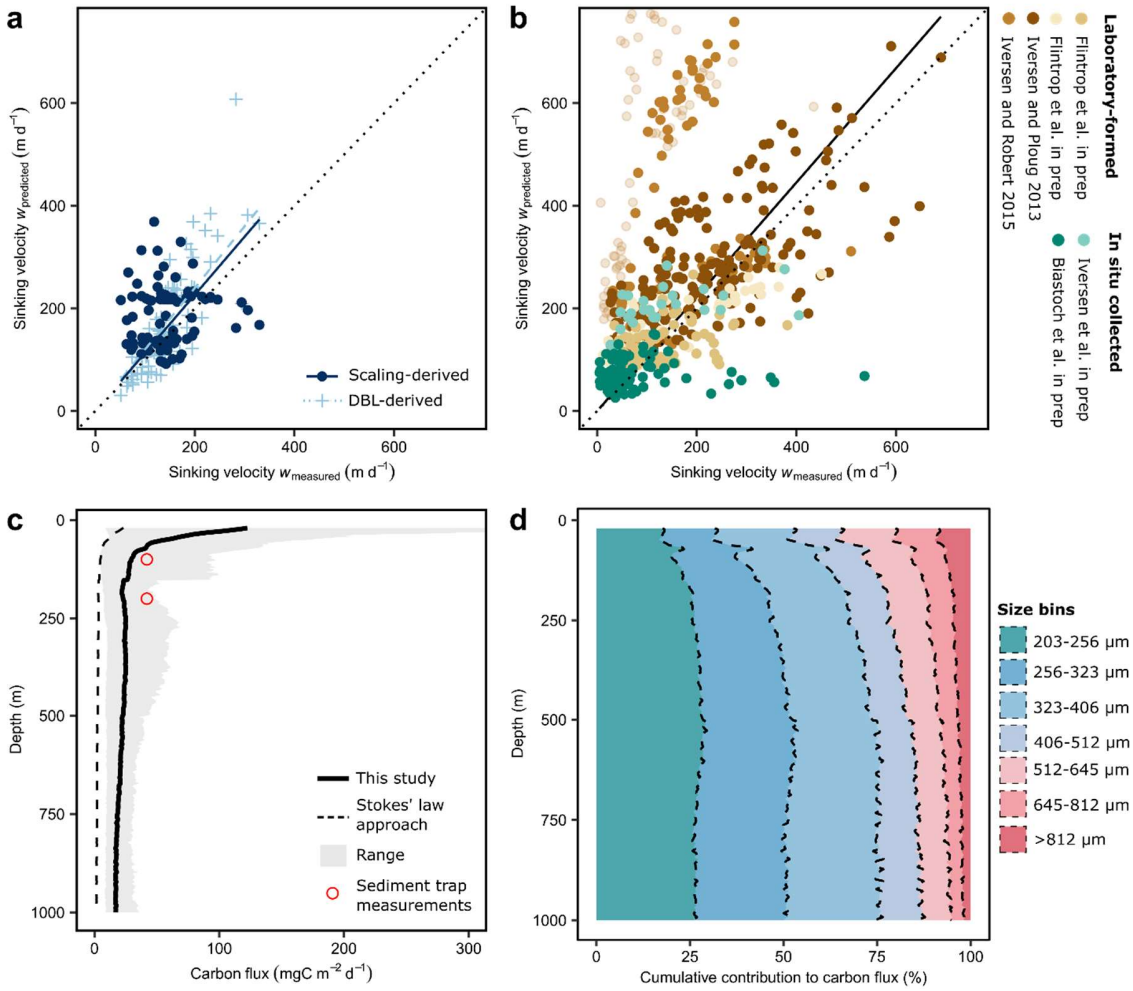

Figure 5. a) Measured versus predicted sinking velocity of particles collected during this study. Dark blue dots: sinking velocities when using our size-dependent porosity (φ) relationship (Material and Methods, Eq. 16). Light blue crosses: sinking velocities when using particle-specific porosity calculated from the normalised boundary layer thickness (Material and Methods, Eq. 15). **b)** Measured versus predicted sinking velocity (Supplementary information, Eq. S1) of particles from selected laboratory and field datasets. **c)** Carbon flux calculated using our relationship

(solid line) and Stokes' law approach (dashed line) compared to measured sediment traps fluxes at 100 m and 200 m. **d)** Cumulative contribution of particle size classes to total carbon flux. Regression equations and R2 for Fig. 5a and Fig. 5b in Table S2 und Table S3, respectively.

Discussion

Improved porosity measurement and sinking velocity prediction

We used the independent measurements, (i) aggregate size *d*, (ii) sinking velocity *w*, and (iii) velocity boundary layer thickness δ_s to estimate the drag coefficient C_D, plus (iv) solid hydrated density ρ_{shd} to get an improved measurement of aggregate porosity in relation to aggregate size. We collected particles with a wide range of primary-particle composition, sizes, and sinking velocities that reflect the diversity and heterogeneity of *in situ* formed aggregates and match previously reported values of size and sinking velocity for natural marine aggregates. Visualisation of the flow field around aggregates showed that the fluid boundary layer thickness, drag coefficient, and general flow field did not noticeably differ from that of impermeable spheres with similar Reynolds numbers, suggesting that *in situ* formed aggregates behave according to basic force balances. Deviations in measured sinking velocities seem to stem from the porosity of marine aggregates, which increases with increasing size following a power function (Alldredge and Gotschalk 1988; Iversen and Ploug 2010; Iversen and Robert 2015; Jagt et al. 2018). The increased porosity for large aggregates caused their excess density to decrease noticeably with increasing diameter. This resulted in lower sinking velocities for large aggregates than predicted by Stokes' drag (Kindler et al. 2010). The drag coefficient estimated from the boundary layer thickness scaled with the Reynolds number. As expected from the Reynolds number regime (*Re* =

0.4-5.2), the Stokes' drag $C_D = \frac{24}{Re}$ (Stokes 1851) was not sufficient to predict sinking velocity. The White relationship (Material and Methods, Eq. 11; White [1974]) as well as our best fit of $C_D = 24/Re^{0.8}$ (Eq. 1) yielded a significant improvement. A similar fit was also found through theoretical approximation by (Jiang and Logan 1991) $C_D = 29.03/Re^{0.87}$). By applying the drag as well as the porosity relationships, the controlling variables can be reduced to diameter, solid hydrated density, gravitational acceleration, water viscosity and density. Knowing these parameters, the sinking velocity of marine aggregates can be calculated in a straightforward manner by combining equations 2, 3, and 8 (giving Eq. 14 [Material and Methods]) as presented in Fig. 5.

Importance of aggregate composition and density

Even though the new parameterization predicts the magnitude and trends of sinking velocities well, larger uncertainties were observed. These were mainly caused by large variability in the solid hydrated density, showing that despite the comparatively low content of solids in marine aggregates, solid hydrated density contributes significantly to the sinking behaviour of marine snow. Solids can affect sinking of marine aggregates in two major ways: the density of solid components affects marine snow by increasing their mass, i.e., excess density (Kindler et al. 2010). At the same time, the shape and properties of solids affect how tightly they can be packed within an aggregate (the compactness) and directly affect the porosity of the aggregate. Average solid hydrated density of aggregates is likely determined by the make-up of the phytoplankton community (Iversen and Ploug 2010; Laurenceau-Cornec et al. 2015; Engel et al. 2009) and lithogenic ballasting minerals (Jagt et al. 2018, Iversen and Robert 2015). It remains a task for future studies to investigate the regulatory mechanisms for solid hydrated density. Until then,

328 literature values can be used to infer sinking velocity from our global porosity scaling (Table S5).
329 Furthermore, we did not find any indication that irregularities in aggregate shape influenced the
330 drag coefficient, even when comparing between aggregate types and to agar spheres (Fig. 5). This
331 supports previous studies which found that shape, permeability, and surface roughness are poor
332 predictors of sinking velocity (Williams 1966; Matsumoto and Suganuma 1977; Baba and Komar
333 1981; Alldredge and Gotschalk 1988; Li and Logan 2001).
334
335 Overall, we did not find any difference in physical properties, including sinking behaviour,
336 between *in situ* formed aggregates and impermeable agar spheres, except that agar spheres are
337 not fractal and therefore porosity did not increase with increasing agar sphere size. This implies
338 that the sinking velocity of marine aggregates can be predicted via the basic force balance
339 equation once the solid hydrated density is known and the size-porosity relationship taken into
340 account. Furthermore, the flow fields around *in situ* collected particles and agar spheres had
341 matching magnitudes and symmetries at similar Reynolds numbers. Even though we cannot rule
342 out that aggregates may be permeable at microscales, this shows that permeability of the types
343 of aggregates we collected is too low to affect their hydrodynamics and sinking velocity, despite
344 their high porosities. Still even a low degree of permeability not detectable at the resolution
345 investigated here could affect solute exchange and microbial colonization. Aggregate
346 impermeability can be explained by high concentrations of transparent exopolymer particles
347 (TEP) that may limit advection, but not diffusion, within aggregates (Ploug et al. 2008). TEP is also
348 the most likely reason that large aggregates, albeit being highly porous, are not permeable, as
349 they occupy the vast majority of the pore space, and constitute a much larger amount of the "non-

fluid" fraction than solid components (Passow 2002; Engel et al. 2002; Simon et al. 2002). This suggests that *in situ* aggregates are mainly diffusive systems where any mass transport to or from the aggregates has to occur across the diffusive boundary layer.

Formulating a global scaling relationship between particle size and carbon flux

Because of the relative ease of imaging particles with bio-optical systems compared to measuring the sinking velocity and carbon content of individual particles, accurately estimating C flux from images has become the "holy grail" of modelling marine carbon cycling. This requires two basic assumptions: 1. That we can relate sinking velocity to size, and 2. that we can accurately predict carbon content based on aggregate size. For the longest time, it was assumed that aggregate size and sinking velocity scale according to a quadratic power function, but while this holds generally true for laboratory-formed aggregates, it has become increasingly clear that this relationship is much weaker for *in situ* aggregates (Iversen and Lampitt 2020; Williams and Giering 2022). With our approach we can provide a mechanistic explanation for this observation, because, once we included variable solid hydrated density and our size-to-porosity relationship into the force balance equation, we were able to predict sinking velocity for both laboratory-formed and *in situ* collected particles. The inclusion of porosity and density distinguishes our relationship from those of Guidi et al. (2008) and Iversen et al. (2010) which were shown to over- or underestimate C flux depending on region and season, and consequently led to the claim that a global scaling was not feasible (Fender et al. 2022). We argue that the reason they were not globally applicable is precisely because of differences in solid hydrated densities between the source communities forming sinking aggregates, and that taking into consideration the density of the solid fraction

negates the necessity of formulating multiple scaling relationships for different regions and/or seasons as postulated by Fender et al. (2022).

Contribution of small particles to export fluxes

Once a size-dependent porosity term is included in the force balance equation, it becomes clear that small particles (here defined as particles < 500 µm, i.e. below the cut-off of what is defined as "marine snow") contribute even more to carbon export than would be expected without considering size-dependent changes in aggregate porosity. We found that small particles, due to their larger carbon-to-volume ratios combined with high particle concentrations, contribute 80% of the cumulative C flux in our study area, and 67% globally on average (Fig. 6). Studies examining particle size distributions with bio-optical systems have previously established the significance of small particles (<500 µm) for carbon export fluxes (Bisson et al. 2022, Kiko et al. 2017, Clements et al. 2022, 2023) and matched our results well (Clements et al. 2023), meaning that we can deliver a mechanistic basis for the observed contributions. Our results further show that the relative contribution of small particles to carbon flux is higher in less productive regions, which is in accordance with Clements et al. (2023), who hypothesize that the apparent correlation with sinking flux can be partially attributed to differences in community structure, such as cell sizes in the initial plankton assemblage. Our results further highlight the importance of camera systems for particle profiling over direct measurements, as particles < 500 µm can only barely be seen with the naked eye. Another advantage of UVPs that can be exploited further is that mean grey values of the imaged particles can potentially be correlated with their porosities. We extracted the mean grey values (ranging from zero to 255, which 0 being black and 255 being white) from images of particles taken under the microscope and found that the proportion of solid matter increased

exponentially with decreasing mean grey value. This conforms to what would intuitively be assumed due to lower amounts of pore space (equaling a low mean grey value) in denser particles (Fig. S3b).

While we observed an overall good agreement of our relationships with measured carbon fluxes, it is important to acknowledge certain limitations. During our measurements of some individual particles, we noticed a substantial alteration of porosity towards lower values, which may introduce some uncertainty. Additionally, recent publications have highlighted the significant impact of ocean stratification (beyond pycnoclines) on particle settling velocity, influenced by drag enhancement and delayed buoyancy adaptation (Ahmerkamp et al. 2022). These processes are likely to further shift carbon fluxes towards smaller particles and should be taken into consideration in future studies.

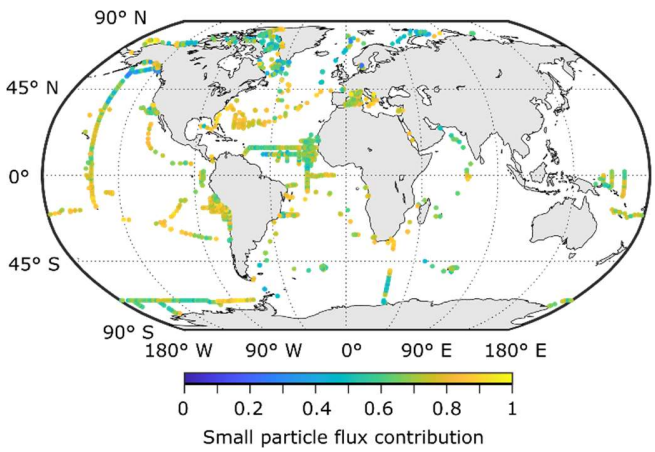

Figure 6. Relative contribution of small particles (< 500 µm) to total carbon flux at the base of the annual mean mixed layer.

Material and Methods

Aggregate collection

Aggregates were collected non-destructively with a Marine Snow Catcher (MSC; Riley et al. 2010) at depths between 20-150 m and left to settle on deck for 5-10 h. Hereafter, single aggregates were picked from the base of the MSC with a wide mouth bore pipette and gently transferred to a vertical flow system to record the size, sinking velocity and flow field around each aggregate. The flow system was modified from Ploug and Jørgensen (1999) to maximize laminarity of the water flow (Fig. 1a-c). The water in the vertical flow system was collected from the same MSC deployment as the aggregates, GF/F-filtered (mean pore size ~0.75 µm), and kept at a constant temperature of 18.2°C (±0.2°C). In addition to collecting natural, in situ formed particles, we created agar spheres made up of 1% agar (wt/wt) mixed with 1% yeast (wt/wt) dissolved in seawater. They were used as model aggregates for impermeable, perfect spheres where solute and gas exchange between the interior and the ambient water occurs via diffusion only. Spheres were formed by dripping the agar solution into a layer of paraffin oil and letting the spheres settle out into an underlying layer of filtered seawater (Cronenberg 1994; Ploug et al. 2002). Agar spheres were immersed in water of equal density as used for the experiments for at least 10 minutes before use to allow salt to diffuse between the ambient and pore water until equilibrium was reached.

Particle Image Velocimetry

For Particle Image Velocimetry (PIV), the water reservoir of the vertical flow system was seeded

with polyamide particles with a mean diameter of 5 µm and a density of 1.1 g/cm^3 (ILA 5150 GmbH) to track the velocity and direction of water flow around the aggregates. The center section of the flow chamber was illuminated with a green LED Pulsing System (LPS, ILA 5150 GmbH) attached to an LED head with optics to create a vertical, 500 µm-wide light sheet illuminating the flow chamber (Fig. 1a-b). The LPS was pulsed at frequencies ranging from 20-30 Hz depending on the flow velocity. The upward flow in the vertical flow system was adjusted until aggregates remained suspended at a distance of approximately 3-5 aggregate diameters above the net of the vertical flow system to eliminate any interaction between surfaces. A series of at least 150 images was recorded with a camera (µEye CP, IDS Imaging Development Systems GmbH), with an attached macro zoom telecentric lens (computar, TEC-V7X, 47.65 - 106.26 mm). The camera was triggered by the LPS, i.e., the frame rate was automatically adjusted according to the LED pulse frequency.

PIV recordings were analysed with the software PivView (PivTech GmbH). Pictures were divided into interrogation windows with an area of 32 pixels each and a 50% overlap. It was qualitatively ensured that each interrogation window contained at least five individual PIV beads. Cross-correlation of each interrogation window between two consecutive images was performed using a discrete fast Fourier transform following the Wiener–Khinchin theorem. To maximize spatial resolution, multi-grid refinement analysis was performed (Raffel et al. 2018). The result was a 2-dimensional velocity matrix with a size of 16 px × 16 px at a resolution of 7 µm/px. The procedure was repeated for at least 80 consecutive images using a batch script. Further processing was performed in Matlab 2015b (The Mathworks, Inc.). Although marine aggregates were mostly

stable within the imposed flow conditions, slight movements in the range of a few pixels were observed. To avoid any blurring while averaging, the movement of the aggregate was corrected using a detection algorithm to re-center the aggregate. For this, PIV seeding was filtered from the raw images using a 2-dimensional median filter with a pixel size of 6 px × 6 px. Subsequently, the image was binarised and the edges of the aggregate were traced. The aggregate was cropped and a cross correlation analysis with the subsequent images was performed to determine the aggregate movement.

Based on the position of the center of gravity, a velocity matrix stack composed of the 80 instantaneous velocity measurements was created with the centered aggregate. Finally, the velocity matrix stack was averaged and the position of the aggregate was masked. Aggregates that exceeded a movement of 20 pixels in horizontal or vertical direction within 2-3 seconds of every possible image sequence were excluded from further analysis. Fluid boundary layer thickness was determined from the averaged magnitude of the flow field. For that, a horizontal cross section was extracted along the equator of the aggregate. The undisturbed maximum velocity along the cross section is equal to the terminal sinking velocity of the aggregate. We then defined the fluid boundary layer as the distance between the aggregate surface and the point where the velocity increases to 90% of the terminal velocity.

Aggregate properties

We measured properties relating to the sinking, porosity and shape of marine aggregates to relate them to each other and to numerically describe aggregate sinking behaviour. Selected properties

including sinking velocity, size, shape factors, solid hydrated density and fluid boundary layer thickness were measured directly, while porosity, excess density and drag coefficient were derived as described in the following. Particle size was measured in two different ways: i) equivalent circular diameter (ECD) of aggregates was calculated from the two-dimensional projected area of aggregates as determined by the edge detection algorithm described above, ii) the x-axis diameter was extracted from images of the PIV recording as the diameter of the particle that is perpendicular to the falling direction. Because the x-axis diameter has a direct impact on the aggregate flow field and is a common input parameter for many hydrodynamic equations, e.g., the drag coefficient (White 1974), we used the x-axis diameter as the length measure for the aggregates throughout this manuscript.

For comparison to previous sinking velocity measurements, sinking velocity of aggregates was also directly determined in the flow chamber by dividing the flow rate by the cross-sectional area of the flow chamber. For this, sinking velocity was recorded for aggregates suspended 3-5 diameters above the net at the height where images were taken for PIV, and one diameter above the net as recommended by Ploug et al. (2010) according to Ploug and Jørgensen (1999). PIV results indicated that the flow field around the aggregates was affected by the proximity to the surface. Therefore, PIV measurements were recorded with the aggregates suspended at least 3-5 diameters above the net in order to ensure an undisturbed flow field. After recordings in the vertical flow system, aggregates were transferred to Utermöhl chambers (Utermöhl 1931) and imaged using brightfield and phase-contrast microscopy at 100x-400x magnification for high-resolution imaging of aggregate composition, type, and structure. To maximize image resolution,

images taken at different depths of field were stacked with Zerene Stacker (Zerene Systems LLC).

The terminal settling velocity w (cm s^{-1}) of objects in the water column is determined through the equilibrium of forces acting upon them. For sinking objects, the dominant force is the gravitational force (F_G), pointing downwards

$$F_G = \rho_p B g \qquad 5$$

Where ρ_p is the particle density (g cm^{-3}), B the biovolume (cm^3) and g is gravitational acceleration (981 cm s^{-1}). The gravitational force is reduced through the upward pointing Archimedean buoyancy force

$$F_B = \rho_W B g \qquad 6$$

and the drag force

$$F_D = 0.5 C_D \rho_W A w^2 \qquad 7$$

Where ρ_w is the water density (g cm^{-3}), A is the area perpendicular to the settling vector (cm^2) and C_D is the drag coefficient. For spherical objects, Stokes (1851) expressed the drag coefficient as a function of the Reynolds number

$$C_D = \frac{24}{Re} \qquad 8$$

with Reynolds number

$$Re = wd\frac{\rho_w}{\eta} \qquad 9$$

where d is the x-axis diameter (cm) and η is the dynamic viscosity of seawater (g cm^{-1} s^{-1}). By substituting Eq. 5-9 into the force balance equation: $0=F_G-F_B-F_A$, the theoretical settling velocities of spherical particles, or aggregates, can be estimated as

$$w = \frac{d^2 g(\rho_p - \rho_w)}{18\eta} \quad 10$$

The theoretical settling velocity w has only a limited validity for creeping flow conditions of Re << 1. However, marine particles usually fall into an intermediate range of 0.1 < Re < 100 (e.g., Alldredge and Gotschalk 1988; Engel et al. 2009; Laurenceau-Cornec et al. 2020). To increase the range of validity the drag coefficient can be iteratively corrected using the equation after White (1974)

$$C_D = \left(\frac{24}{Re}\right) + \left(\frac{6}{1 + Re^{0.5}}\right) + 0.4 \quad 11$$

A major challenge associated to the prediction of marine particle settling velocity is to determine the excess density $\Delta\rho = \rho_s - \rho_w$ which depends on the porosity of the particle, i.e., the ratio of voids to total volume, and the solid hydrated density ρ_{shd}. By applying Eq. 9-11, the excess density can be expressed as

$$\Delta\rho = \frac{C_D\, \rho_w\, w^2}{\frac{4}{3} g d} = (1 - \varphi)\rho_{shd} + \rho_w \varphi - \rho_w \quad 12$$

In order to reduce the number of unknowns in the equations above, we directly measured ρ_{shd} using the linear gradient method (see section below). Additionally, we independently derived the drag coefficient from the fluid boundary layer thickness obtained from the PIV measurements using empirical relationships according to Moradi et al. (2018): a cubic polynomial function given by

$$C_D = a \cdot {\delta_s}^3 + b \cdot {\delta_s}^2{}_s + c \cdot \delta_s + d \quad 13$$

with *a* = 8.8, *b* = -15.1, *c* = 22.3, and *d* = -2.6 was used to mathematically relate the drag coefficient to the fluid boundary layer for 0.02 ≤ Re ≤ 20, where δ_s is the equatorial fluid boundary layer (δ)

normalised by the x-axis diameter (d). Aggregate porosity (φ) was calculated by re-arranging Eq. 12 as follows

$$\varphi = \frac{\Delta\rho + \rho_w - \rho_{shd}}{\rho_w - \rho_{shd}} \qquad 14$$

We further characterised the microstructure of the aggregates by determining their 1- & 2-dimensional fractal numbers DF1 and DF2, respectively. Following Kilps et al. (1994), the 1- and 2-dimensional fractal numbers (DF1 and DF2), were calculated from the slopes of log-log relationships of perimeter and area respectively, against the equivalent circular diameter. To test the impact of aggregate shape on sinking velocities, we used images from the PIV recording to extract the parameters for morphological roughness, textural roughness, and form using the image processing software FIJI/ImageJ (Schindelin et al. 2012). Aspect ratio, area:perimeter, circularity, orientation, convexity, solidity, contour temperature and fractal dimension were analysed using the ImageJ Shape Filter Plugin (Wagner and Lipinski 2013).

The solid hydrated density (ρ_{shd}) of aggregates was determined in a seven-layer density gradient made with dilutions from Ludox TM colloidal silica (Sigma-Aldrich), sucrose and distilled water (following Gärdes et al. [2011] and Iversen and Robert [2015] who modified the method from Schwinghamer et al. [1991], and Feinberg and Dam [1998]). The dilutions ranged in density from 1.155 to 1.428 g cm^{-3}. Starting with the densest solution, 2 ml of each dilution were gently transferred to 15 ml centrifuge tubes (Corning) and topped with 2 ml of GF/F-filtered seawater. Single aggregates were gently added to the topmost layer of the density gradient using a wide-mouth bore pipette and left to settle into the gradient at 4°C overnight. The following day, 1 ml was sampled from the layer the aggregate had settled into, which is representative of the density

of the solid components of the aggregate. Samples were kept at 4°C in sealed 1 ml-tubes until the end of the cruise, and measured with a density meter (DMA 38, Anton Paar) back in the home laboratory. Because the aggregates were destroyed in the process, this measurement was done at the very end.

Sinking velocity and carbon flux predictions

Sinking velocity comparisons

To test the suitability of our fitted relationship for predicting sinking velocity, we compared the experimentally measured and the predicted sinking velocities of the collected particles, once with the porosity calculated based on the boundary layer-scaling

$$w = d^2 g \left(\left(\frac{\frac{(a{\delta_s}^3 + b{\delta_s}^2{}_s + c\delta_s + d)\rho_w w^2}{4/3gd}}{(\rho_w - \rho_s)} \right) - \rho_w \right) \Big/ 18\eta \qquad 15$$

which combines equations 10, 12 and 13 to predict sinking velocity based on the normalized boundary layer thickness as measured using PIV, and once with the porosity calculated using our best fit between porosity and size, specific for each aggregate type

$$w = \frac{d^2 g(1 - (-ad^b + 1)\rho_s + (-ad^b + 1 - 1)\rho_w}{18\eta} \qquad 16$$

which combines equations 3 and 10 to predict sinking velocity based on the fitted regression between aggregate size and porosity, which was independently derived from the boundary layer-inferred drag coefficient. To test the applicability for other datasets from different regions and origins, we collected datasets with known water density and, experimentally measured sinking

velocity, size and solid hydrated density ρ_{shd} and used our relationship to calculated porosity, based on which excess density and sinking velocity were consequently calculated (Eq. 16).

Sediment trap deployment and particle-specific carbon content

To measure *in situ* carbon fluxes, we deployed two drifting sediment traps for a duration of 22 hours each. The drifting sediment trap consisted of one trap station each at depths of 100 & 200 m equipped with four collection cylinders. Material from one trap tube per depth was fixed with 1.4% mercury chloride and stored at 4°C for later determination of mass fluxes of carbon, nitrogen, biogenic opal, calcium carbonate, and lithogenic (non-biogenic) material. In trap 1, two collection cylinders per depth were equipped with a viscous cryogel (Tissue-Tek, Sakura Finetek) to structurally preserve aggregates in order to determine their abundance & size spectra, and in combination with measured carbon fluxes, determine size-specific carbon content. Aggregates collected in the gel cups were imaged on board, and images were subsequently processed with the image processing software FIJI/ImageJ (Schindelin et al. 2012).

Particle sizes and numbers across the water column were recorded with the Underwater Vision Profiler 5hd (UVP 5hd; Picheral et al. 2010; HYDROPTIC, France) in a total of 72 profiles. The UVP was mounted inside the CTD frame and operated in autonomous pressure mode. Images were acquired with a maximum frequency of 20 Hz during every downcast. The sampling volume was approximately 1 litre, with a particle quantification threshold of 2 pixels (~80 µm ESD). Post-processing was accomplished using the ImageJ based software Zooprocess (Gorsky et al. 2010), as well as the Ecotaxa platform and the Ecopart export tool (Picheral et al. 2017). We re-interpolated the data onto 1 m steps within the depth range of 20 m to 500 m. Subsequently, we

categorised the particles into the same size bins as above. We then calculated the average of all N=72 profiles and integrated the size-specific carbon fluxes. This integration allowed us to calculate depth profiles of carbon fluxes

$$J(z) = \frac{1}{N} \iint_{d_0}^{d_1} B(d,z) m(d,z) U(d,z) \mathrm{d}d\mathrm{d}n \qquad 17$$

Where z is water depth (m), U(d) the particle settling velocity, r0 = 128 µm and r1 = 2024 µm are the lower and upper limits for integration. The settling velocity was calculated by applying our newly derived size-porosity relationship (Eq. 2), combined with Eq. 3 and Eq. 8 (giving Eq. 14).

Global contribution of **small** particles to export flux

We obtained a comprehensive dataset of 13,291 global under-water-vision (UVP)-based particle profiles from the publicly available ECOTAXA database (Last visit: 7/21/2023). After a rigorous initial quality check and filtering process targeting profiles below 1000 m depths, our dataset was significantly refined, leaving us with 2,669 high-quality underwater particle profiles. We utilised Eq. 2 to calculate the flux at a depth of 500 m. The only difference was in the excess density calculation, given the absence of a global dataset on solid hydrated density. Nevertheless, we found a remarkably strong direct relationship between porosity and excess density: $\Delta\rho = 0.08 \cdot (1-\phi)^{0.73}$, which we employed in our calculations. To gain insight into the impact of small particles, we calculated the ratio of carbon flux induced by particles ranging from 128 µm to 512 µm with the total carbon flux.

Acknowledgments

The authors thank the captain and crew of the B/O Sarmiento de Gamboa for enabling this study. This study was supported by the Helmholtz Association and the Alfred Wegener Institute for Polar and Marine Research, the DFG-Research Center/Cluster of Excellence “The Ocean in the Earth System”, and the Max Planck Institute for Marine Microbiology. SHA acknowledges funding for the MARMA project by the Max Planck Society and the MATIC project by Novo Nordisk Fonden. HPG acknowledges funding from DFG projects GR1540/28-1, GR1540/37-1 and IV124/3-1/ This publication is supported by the HGF Young Investigator Group SeaPump “Seasonal and regional food web interactions with the biological pump”: VH-NG-1000.

Conflict of interest

The authors declare no conflict of interest.

References

Ahmerkamp, S., F. M. Jalaluddin, Y. Cui, and others. 2022. Simultaneous visualization of flow fields and oxygen concentrations to unravel transport and metabolic processes in biological systems. Cell Rep. Methods **2**: 100216. doi:10.1016/j.crmeth.2022.100216

Alldredge, A. L., and C. Gotschalk. 1988. In situ settling behavior of marine snow. Limnol. Oceanogr. **33**: 339–351. doi:10.4319/lo.1988.33.3.0339

Azetsu-Scott, K., and B. D. Johnson. 1992. Measuring physical characteristics of particles: a new method of simultaneous measurement for size, settling velocity and density of constituent matter. Deep-Sea Res. Part I-Oceanogr. Res. Pap. **39**: 1057–1066. doi:10.1016/0198-0149(92)90039-V

Azetsu-Scott, K., and U. Passow. 2004. Ascending marine particles: Significance of transparent exopolymer particles (TEP) in the upper ocean. Limnol. Oceanogr. **49**: 741–748. doi:10.4319/lo.2004.49.3.0741

Baba, J., and P. D. Komar. 1981. Settling velocities of irregular grains at low Reynolds numbers. J. Sediment. Res. **51**: 121–128. doi:10.1306/212F7C25-2B24-11D7-8648000102C1865D

Bach, L. T., T. Boxhammer, A. Larsen, N. Hildebrandt, K. G. Schulz, and U. Riebesell. 2016. Influence of plankton community structure on the sinking velocity of marine aggregates. Global Biogeochem. Cycles **30**: 2016GB005372. doi:10.1002/2016GB005372

Bisson, K. M., R. Kiko, D. A. Siegel, L. Guidi, M. Picheral, E. Boss, and B. B. Cael. 2022. Sampling uncertainties of particle size distributions and derived fluxes. Limnol. Oceanogr. Methods **20**: 754–767. doi:10.1002/lom3.10524

Bruland, K. W., and M. W. Silver. 1981. Sinking rates of fecal pellets from gelatinous zooplankton (Salps, Pteropods, Doliolids). Mar. Biol. **63**: 295–300. doi:10.1007/BF00395999

Cavan, E. L., M. Trimmer, F. Shelley, and R. Sanders. 2017. Remineralization of particulate organic carbon in an ocean oxygen minimum zone. Nat. Commun. **8**: 14847. doi:10.1038/ncomms14847

Clements, D. J., S. Yang, T. Weber, A. M. P. McDonnell, R. Kiko, L. Stemmann, and D. Bianchi. 2022. Constraining the Particle Size Distribution of Large Marine Particles in the Global Ocean With In Situ Optical Observations and Supervised Learning. Global Biogeochem. Cycles **36**: e2021GB007276. doi:10.1029/2021GB007276

Clements, D. J., S. Yang, T. Weber, A. M. P. McDonnell, R. Kiko, L. Stemmann, and D. Bianchi. 2023. New Estimate of Organic Carbon Export From Optical Measurements Reveals the Role of Particle Size Distribution and Export Horizon. Global Biogeochem. Cycles **37**: e2022GB007633. doi:10.1029/2022GB007633

Cole, M. C., P. Lindeque, E. S. Fileman, J. Clark, C. Lewis, C. Halsband, and T. S. Galloway. 2016. Microplastics Alter the Properties and Sinking Rates of Zooplankton Faecal Pellets. Environ. Sci. Technol. **50**: 3239–3246. doi:10.1021/acs.est.5b05905

Cronenberg, C. C. H. 1994. Biological engineering on a microscale: Biofilms investigated with needle-type glucose sensors. University of Amsterdam.

Dillon, W. P. 1964. Flotation Technique for Separating Fecal Pellets and Small Marine Organisms from Sand. Limnol. Oceanogr. **9**: 601–602. doi:10.4319/lo.1964.9.4.0601

Dunbar, R. B., and W. H. Berger. 1981. Fecal pellet flux to modern bottom sediment of Santa Barbara Basin (California) based on sediment trapping. GSA Bulletin **92**: 212–218. doi:10.1130/0016-7606

Engel, A., M. Meyerhöfer, and K. von Bröckel. 2002. Chemical and Biological Composition of Suspended Particles and Aggregates in the Baltic Sea in Summer (1999). Estuar. Coast. Shelf Sci. **55**: 729–741. doi:10.1006/ecss.2001.0927

Engel, A., and M. Schartau. 1999. Influence of transparent exopolymer particles (TEP) on sinking velocity of Nitzschia closterium aggregates. Mar. Ecol. Prog. Ser. **182**: 69–76. doi:10.3354/meps182069

Engel, A., J. Szlosek, L. Abramson, Z. Liu, and C. Lee. 2009. Investigating the effect of ballasting by CaCO3 in Emiliania huxleyi: I. Formation, settling velocities and physical properties of aggregates. Deep Sea Res. Part II Top. Stud. Oceanogr. **56**: 1396–1407. doi:10.1016/j.dsr2.2008.11.027

Feinberg, L., and H. Dam. 1998. Effects of diet on dimensions, density and sinking rates of fecal pellets of the copepod Acartia tonsa. Mar. Ecol. Prog. Ser. **175**: 87–96. doi:10.3354/meps175087

Fender, C. K., T. B. Kelly, L. Guidi, M. D. Ohman, M. C. Smith, and M. R. Stukel. 2019. Investigating Particle Size-Flux Relationships and the Biological Pump Across a Range of Plankton Ecosystem States From Coastal to Oligotrophic. Front. Mar. Sci. **6**. doi:10.3389/fmars.2019.00603

Fowler, S. W., and L. F. Small. 1972. Sinking Rates of Euphausiid Fecal Pellets. Limnol. Oceanogr. **17**: 293–296. doi:10.4319/lo.1972.17.2.0293

Gärdes, A., M. H. Iversen, H.-P. Grossart, U. Passow, and M. S. Ullrich. 2011. Diatom-associated bacteria are required for aggregation of Thalassiosira weissflogii. ISME J **5**: 436–445. doi:10.1038/ismej.2010.145

Giering, S. L. C., E. L. Cavan, S. L. Basedow, and others. 2020. Sinking Organic Particles in the Ocean—Flux Estimates From in situ Optical Devices. Front. Mar. Sci. **6**. doi:10.3389/fmars.2019.00834

Gorsky, G., N. S. Fisher, and S. W. Fowler. 1984. Biogenic debris from the pelagic tunicate, Oikopleura dioica, and its role in the vertical transport of a transuranium element. Estuar. Coast. Shelf Sci. **18**: 13–23. doi:10.1016/0272-7714(84)90003-9

Grossart, H.-P., and H. Ploug. 2001. Microbial degradation of organic carbon and nitrogen on diatom aggregates. Limnol. Oceanogr. **46**: 267–277. doi:10.4319/lo.2001.46.2.0267

Guidi, L., L. Legendre, G. Reygondeau, J. Uitz, L. Stemmann, and S. A. Henson. 2015. A new look at ocean carbon remineralization for estimating deepwater sequestration. Global Biogeochem. Cycles **29**: 1044–1059. doi:10.1002/2014GB005063

Hansen, J. L. S., T. Kiørboe, and A. Alldredge. 1996. Marine snow derived from abandoned larvacean houses: sinking rates, particle content and mechanisms of aggregate formation. Mar. Ecol. Prog. Ser. **141**: 205–215. doi:10.3354/meps141205

Iversen, M. H., N. Nowald, H. Ploug, G. A. Jackson, and G. Fischer. 2010. High resolution profiles of vertical particulate organic matter export off Cape Blanc, Mauritania: Degradation processes and ballasting effects. Deep-Sea Res. Part I-Oceanogr. Res. Pap. **57**: 771–784. doi:10.1016/j.dsr.2010.03.007

Iversen, M. H., and H. Ploug. 2010. Ballast minerals and the sinking carbon flux in the ocean: carbon-specific respiration rates and sinking velocity of marine snow aggregates. Biogeosciences **7**: 2613–2624. doi:10.5194/bg-7-2613-2010

Iversen, M. H., and H. Ploug. 2013. Temperature effects on carbon-specific respiration rate and sinking velocity of diatom aggregates – potential implications for deep ocean export processes. Biogeosciences **10**: 4073–4085. doi:10.5194/bg-10-4073-2013

Iversen, M. H., and M. L. Robert. 2015. Ballasting effects of smectite on aggregate formation and export from a natural plankton community. Mar. Chem. **175**: 18–27. doi:10.1016/j.marchem.2015.04.009

Jackson, G. A., and D. M. Checkley. 2011. Particle size distributions in the upper 100m water column and their implications for animal feeding in the plankton. Deep-Sea Res. Part I-Oceanogr. Res. Pap. **58**: 283–297. doi:10.1016/j.dsr.2010.12.008

Jagt, H. van der, C. Friese, J.-B. W. Stuut, G. Fischer, and M. H. Iversen. 2018. The ballasting effect of Saharan dust deposition on aggregate dynamics and carbon export: Aggregation, settling, and scavenging potential of marine snow. Limnol. Oceanogr. **63**: 1386–1394. doi:10.1002/lno.10779

Karthäuser, C., S. Ahmerkamp, H. K. Marchant, and others. 2021. Small sinking particles control anammox rates in the Peruvian oxygen minimum zone. Nat. Commun. **12**: 3235. doi:10.1038/s41467-021-23340-4

Kiko, R., A. Biastoch, P. Brandt, and others. 2017. Biological and physical influences on marine snowfall at the equator. Nat. Geosci. **10**: 852–858. doi:10.1038/ngeo3042

Kilps, J. R., B. E. Logan, and A. L. Alldredge. 1994. Fractal dimensions of marine snow determined from image analysis of in situ photographs. Deep-Sea Res. Part I-Oceanogr. Res. Pap. **41**: 1159–1169. doi:10.1016/0967-0637(94)90038-8

Kindler, K., A. Khalili, and R. Stocker. 2010. Diffusion-limited retention of porous particles at density interfaces. Proc. Natl. Acad. Sci. U.S.A. **107**: 22163–22168. doi:10.1073/pnas.1012319108

Klawonn, I., S. Van den Wyngaert, M. H. Iversen, and others. 2023. Fungal parasitism on diatoms alters formation and bio–physical properties of sinking aggregates. Commun. Biol. **6**: 1–14. doi:10.1038/s42003-023-04453-6

Komar, P. D., A. P. Morse, L. F. Small, and S. W. Fowler. 1981. An analysis of sinking rates of natural copepod and euphausiid fecal pellets1. Limnol. Oceanogr. **26**: 172–180. doi:10.4319/lo.1981.26.1.0172

Laurenceau-Cornec, E. C., F. A. C. Le Moigne, M. Gallinari, B. Moriceau, J. Toullec, M. H. Iversen, A. Engel, and C. L. De La Rocha. 2020. New guidelines for the application of Stokes' models to the sinking velocity of marine aggregates. Limnol. Oceanogr. **65**: 1264–1285. doi:10.1002/lno.11388

Laurenceau-Cornec, E., T. Trull, D. Davies, C. De La Rocha, and S. Blain. 2015. Phytoplankton morphology controls on marine snow sinking velocity. Mar. Ecol. Prog. Ser. **520**: 35–56. doi:10.3354/meps11116

Li, X.-Y., and B. E. Logan. 2001. Permeability of Fractal Aggregates. Water Res. **35**: 3373–3380. doi:10.1016/S0043-1354(01)00061-6

Matsumoto, K., and A. Suganuma. 1977. Settling velocity of a permeable model floc. Chem. Eng. Sci. **32**: 445–447. doi:10.1016/0009-2509(77)85009-4

McDonnell, A. M. P., and K. O. Buesseler. 2010. Variability in the average sinking velocity of marine particles. Limnol. Oceanogr. **55**: 2085–2096. doi:10.4319/lo.2010.55.5.2085

Milner, S., G. Langer, M. Grelaud, and P. Ziveri. 2016. Ocean warming modulates the effects of acidification on Emiliania huxleyi calcification and sinking. Limnol. Oceanogr. **61**: 1322–1336. doi:10.1002/lno.10292

Moradi, N., B. Liu, M. Iversen, M. M. Kuypers, H. Ploug, and A. Khalili. 2018. A new mathematical model to explore microbial processes and their constraints in phytoplankton colonies and sinking marine aggregates. Sci. Adv. **4**: eaat1991. doi:10.1126/sciadv.aat1991

Passow, U. 2002. Production of transparent exopolymer particles (TEP) by phyto- and bacterioplankton. Mar. Ecol. Prog. Ser. **236**: 1–12. doi:10.3354/meps236001

Picheral, M., S. Colin, and J.-O. Irisson. 2017. EcoTaxa, a Tool for the Taxonomic Classification of Images.

Picheral, M., L. Guidi, L. Stemmann, D. M. Karl, G. Iddaoud, and G. Gorsky. 2010. The Underwater Vision Profiler 5: An advanced instrument for high spatial resolution studies of particle size spectra and zooplankton. Limnol. Oceanogr. Methods **8**: 462–473. doi:10.4319/lom.2010.8.462

Ploug, H., H. P. Grossart, F. Azam, and B. B. Jørgensen. 1999. Photosynthesis, respiration, and carbon turnover in sinking marine snow from surface waters of Southern California Bight: Implications for the carbon cycle in the ocean. Mar. Ecol. Prog. Ser. **179**: 1–11. doi:10.3354/meps179001

Ploug, H., S. Hietanen, and J. Kuparinen. 2002. Diffusion and advection within and around sinking, porous diatom aggregates. Limnol. Oceanogr. **47**: 1129–1136. doi:10.4319/lo.2002.47.4.1129

Ploug, H., M. H. Iversen, and G. Fischer. 2008. Ballast, sinking velocity, and apparent diffusivity within marine snow and zooplankton fecal pellets: Implications for substrate turnover by attached bacteria. Limnol. Oceanogr. **53**: 1878–1886. doi:10.4319/lo.2008.53.5.1878

Ploug, H., and B. B. Jørgensen. 1999. A net-jet flow system for mass transfer and microsensor studies of sinking aggregates. Mar. Ecol. Prog. Ser. **176**: 279–290. doi:10.3354/meps176279

Ploug, H., A. Terbrüggen, A. Kaufmann, D. Wolf-Gladrow, and U. Passow. 2010. A novel method to measure particle sinking velocity in vitro, and its comparison to three other in vitro methods. Limnol. Oceanogr. Methods **8**: 386–393. doi:10.4319/lom.2010.8.386

Raffel, M., C. E. Willert, F. Scarano, C. Kähler, S. T. Wereley, and J. Kompenhans. 2018. Particle Image Velocimetry: A Practical Guide, 3rd ed. Springer International Publishing.

Riley, J. S., R. Sanders, C. Marsay, F. a. C. Le Moigne, E. P. Achterberg, and A. J. Poulton. 2012. The relative contribution of fast and slow sinking particles to ocean carbon export. Global Biogeochem. Cycles **26**. doi:10.1029/2011GB004085

Schindelin, J., I. Arganda-Carreras, E. Frise, and others. 2012. Fiji: an open-source platform for biological-image analysis. Nat. Methods **9**: 676–682. doi:10.1038/nmeth.2019

Schwinghamer, P., D. M. Anderson, and D. M. Kulis. 1991. Separation and concentration of living dinoflagellate resting cysts from marine sediments via density-gradient centrifugation. Limnol. Oceanogr. **36**: 588–592. doi:10.4319/lo.1991.36.3.0588

Silver, M. W., M. M. Gowing, D. C. Brownlee, and J. O. Corliss. 1984. Ciliated protozoa associated with oceanic sinking detritus. Nature **309**: 246–248. doi:10.1038/309246a0

Simon, M., H.-P. Grossart, B. Schweitzer, and H. Ploug. 2002. Microbial ecology of organic aggregates in aquatic ecosystems. Aquat. Microb. Ecol. **28**: 175–211. doi:10.3354/ame028175

Small, L. F., and S. W. Fowler. 1973. Turnover and vertical transport of zinc by the euphausiid Meganyctiphanes norvegica in the Ligurian Sea. Mar. Biol. **18**: 284–290. doi:10.1007/BF00347790

Small, L. F., S. W. Fowler, and M. Y. Ünlü. 1979. Sinking rates of natural copepod fecal pellets. Mar. Biol. **51**: 233–241. doi:10.1007/BF00386803

Stemmann, L., G. A. Jackson, and D. Ianson. 2004. A vertical model of particle size distributions and fluxes in the midwater column that includes biological and physical processes—Part I: model formulation. Deep-Sea Res. Part I-Oceanogr. Res. Pap. **51**: 865–884. doi:10.1016/j.dsr.2004.03.001

Stokes, G. G. 1851. On the Effect of the Internal Friction of Fluids on the Motion of Pendulums. Trans. Cambridge Philos. Soc. **9**: 8. doi:10.1017/CBO9780511702266.002

The Math Works, Inc. MATLAB, version 2015b. Natick, MA: The Math Works, Inc., 2020. Accessed Aug 28, 2023. https://www.mathworks.com/

Volk, T., and M. I. Hoffert. 1985. The Carbon Cycle and Atmospheric CO2: Natural Variations Archean to Present E.T. Sundquist and W.S. Broecker [eds.]. Geophys. Monogr. Ser. **32**: 99–110. doi:10.1029/GM032p0099

Wagner, T., and H. Lipinsky. 2013. IJBlob: An ImageJ Library for Connected Component Analysis and Shape Analysis. J. Open Res. Softw. **1**: e6. doi:10.5334/jors.ae

White, F. M. 1991. Viscous Fluid Flow, McGraw-Hill.

Wiebe, P. H., S. H. Boyd, and C. Winget. 1976. Particulate matter sinking to the deep-sea floor at 2000 M in the Tongue of the Ocean, Bahamas, with a description of a new sedimentation trap. J. Mar. Res. **34**: 341–354. doi:10.1575/1912/1792

Williams, W. E. 1966. Boundary effects in Stokes flow. J. Fluid Mech. **24**: 285–291. doi:10.1017/S0022112066000648

Tables

Table 1. Overview of measured parameters for the different aggregate types. "All aggregates" denote the sum of in situ collected particles (excluding agar spheres).

Type	n (#)	d (mm)	w (m d^{-1})	Re	C_D	Δρ (g cm^{-3})	ρ_{shd} (g cm^{-3})	ϕ
All collected particles	81	1.17± 0.6	146.3 ±56	1.8 ±1.1	22.0 ±12.1	0.0051± 0.0046	1.23±0.09	0.977 ±0.02
Phytoplankton aggregates	36	1.36± 0.8	147.3 ±67	2.1 ±1.3	21.6 ±14.2	0.0053 ±0.0060	1.17±0.04	0.976 ±0.03
Ballasted mucous aggregates	22	1.26± 0.4	163.4 ±47	2.1 ±1.0	17.1 ±6.4	0.0044 ±0.0026	1.26±0.05	0.980 ±0.01
Degraded faecal pellets	23	0.84± 0.2	128.3 ±35	1.2 ±0.4	27.5 ±10.3	0.0056 ±0.0030	1.31±0.08	0.974 ±0.01
Agar spheres	13	1.26± 0.3	146.3 ±58	2.1 ±1.3	20.0 ±11.8	0.0027 ±0.0004	1.14±0.02	0.976 ±0.00